 

PACS numbers: 79.20.Eb; 42.55.Lt
DOI: 10.1070/QE2015v045n07ABEH015570

# Pulsed laser ablation of Ni in vacuum and $N_2$ atmosphere at various fluences

Shazia Bashir, Shazaib Khurshid, Mahreen Akram, Nisar Ali, Umm-i-Kalsoom, Shahbaz Ahmad, Daniel Yousaf

*Abstract.* **Mechanisms of Ni ablation in vacuum and $N_2$ atmosphere at various fluences ranging from 2.1 J cm$^{-2}$ to 3.4 J cm$^{-2}$ are studied by using a KrF excimer laser. The formation of various conical microstructures, ripples, large-sized irregular shaped cavities and pits is found. It is shown that no new phases are formed in the case of Ni ablation in vacuum, while new phases of nitrides and nitro-oxides appear in the $N_2$ environment. The microhardness analysis of targets irradiated in vacuum shows a decreasing trend with increasing fluence, whereas in the case of the $N_2$ environment, a monotonic increase in hardness with increasing fluence is observed.**

***Keywords:*** *laser ablation, mechanical properties, grains, ripples.*

## 1. Introduction

Pulsed laser ablation of metals has a vast range of potential applications in the field of laser-based material processing, e.g. pulsed laser deposition of thin films [1, 2], growth of nanostructures [3], synthesis of nanoparticles [4], material surface cleaning [5], etc.

Micro- and nanostructured materials can be used in electronic, fluidic, mechanical and optical devices [6, 7]. Being a transition metal, nickel has significant chemical activity, slow rate of oxidation and is considered the best corrosion-resistant and ferromagnetic material at room temperature. Ni particles are an important magnetic material for storing information. To the best of knowledge, few papers have been published, which report laser ablation of Ni in the ambient environment of nitrogen and in vacuum.

Laser-induced micro- and nanostructuring of Ni surface under different ambient environments has been reported by several groups [8–10]. Excimer lasers are a valuable tool for the fabrication and growth of micro-/nanostructures on the irradiated target surface [7]. The nature and pressure of the ambient environment play a significant role for energy delivery to the target and its modification [11, 12]. Therefore, the role of the ambient environment is critical for micro- and nanostructuring of the material. Preuss et al. [13] investigated the effect of the ambient environment (vacuum and $N_2$ atmosphere) on the ablation efficiency of various metals, such as nickel, molybdenum, copper, indium, gold and tungsten. They suggested that metal ablation in the $N_2$ environment is less efficient than in vacuum due to the shielding effect and enhanced redeposition of the ablated material. Zuhlke et al. [14] reported the formation of self-organised micro- and nanostructured surfaces on Ni via both above-surface growth (ASG) and below-surface growth (BSG) mechanisms using femtosecond laser pulse irradiation. Liu et al. [15] studied the morphological and structural properties of nanoparticles generated by ultrafast laser ablation of Ni. Ni particles are important magnetic materials for information storage. Amoruso et al. [16] presented experimental results and theoretical analysis of ultrashort femtosecond laser ablation of a Ni target.

In the present work we study the effect of laser fluence and ambient environments (vacuum, $N_2$) on the micro- and nanostructuring of Ni surface. Various characterisation techniques like scanning electron microscopy, Raman spectroscopy, X-ray diffraction and microhardness testing have been employed to study the surface, structural and hardness modification of laser irradiated Ni.

## 2. Experimental setup

As a target material we used metal nickel with purity of 99.999%. Cylindrically shaped samples measuring 10×5 mm were grinded, polished and ultrasonically cleaned with deionised water for 30 min. The prepared samples were placed in a stainless-steel vacuum ($10^{-3}$ mbar) chamber.

KrF excimer laser (EX GAM USA 200) radiation with a pulse duration of 20 ns, wavelength of 248 nm and repetition rate of 30 Hz was employed to perform ablation. The excimer laser had a maximum pulse energy of 150 mJ in a rectangular beam of size 11×7 mm. The beam was focused onto the target surface by using a lens with a focal length of 50 cm, at an angle of 90° with respect to its surface. The targets were irradiated at four laser fluences of 2.1, 2.5, 2.9 and 3.4 J cm$^{-2}$ corresponding to laser pulsed energies of 50, 60, 70 and 80 mJ, respectively, with a beam spot size of 0.0235 cm$^2$. Two series of experiments were performed: in vacuum at a pressure of $\sim 10^{-3}$ Torr and in the ambient environment of $N_2$ at a pressure of 100 Torr. All experiments were performed with 1000 pulses of the excimer laser.

Surface morphology of laser-irradiated Ni samples was investigated with a JEOL JSM-6480 LV scanning electron microscope (SEM). Structural analysis was performed using a LABRAM HR800 HORIBA JOBINYVON Raman spectroscope and an X'Pert PRO MPD X-ray diffractometer (XRD). A Zwick/Roell ZHU-5030 microhardness tester was used to

**Shazia Bashir, Mahreen Akram, Shahbaz Ahmad** Centre for Advanced Studies in Physics, GC University Lahore, Pakistan; e-mail: shaziabashir@gcu.edu.pk;
**Shazaib Khurshid, Nisar Ali, Umm-i-Kalsoom** Centre for Advanced Studies in Physics, GC University Lahore, Pakistan; Department of Physics, GC University Lahore, Pakistan;
**Daniel Yousaf** Department of Physics, GC University Lahore, Pakistan

Received 29 May 2014; revision received 19 August 2014
Kvantovaya Elektronika **45** (7) 640–647 (2015)
Submitted in English

measure micro hardness at the periphery of the irradiated samples.

## 3. Results and discussion

Analysis of SEM images (Fig. 1) reveals the variation in the surface morphology of the central ablated region of Ni targets. Figure 1a shows the formation of protruding conical structures with a wide rippled base and a spherical top as well as large-sized irregular shaped cavities, cracks, ridges and conical pits. The inset of Fig. 1a presents a magnified view of the ripples, with an average periodicity of about 2.2 μm at the base of conical microstructures. An increase in the fluence up to 2.5 J $cm^{-2}$ results in an increase in the rippled area, enhanced size and density of irregular shaped cavities, cracks and conical structures. The inset of Fig. 1b shows a magnified view of virtually equidistant ripples (periodicity of 800 nm) at the base of conical structures. A further increase in the fluence up to 2.9 J $cm^{-2}$ (Fig. 1c) leads to an increase in the density of ripples along with the refilling of large-sized irregular shaped cavities. An increase in size and density of conical structures and a decrease in size and density of cracks is also observed. At a maximum fluence of 3.4 J $cm^{-2}$ (Fig. 1d), an enhanced area of ripples, along with an enhanced density of cones, pits, droplets and cracks, is observed.

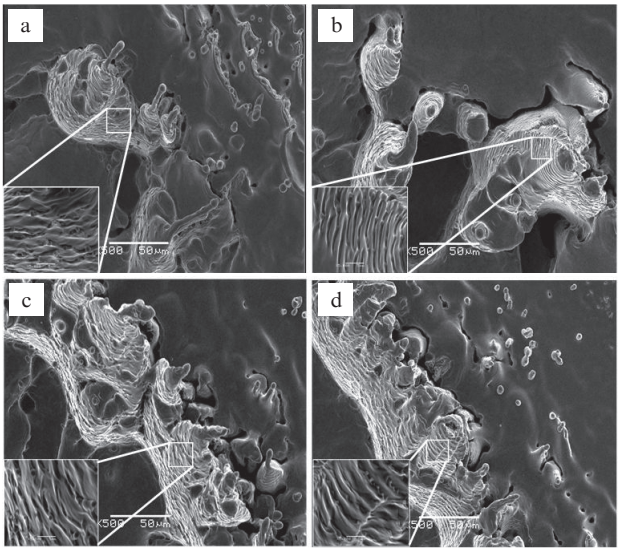


**Figure 1.** SEM images illustrating the formation of laser induced structures in the central ablated area after irradiation of Ni targets in vacuum at laser fluences of (a) 2.1, (b) 2.5, (c) 2.9 and (d) 3.4 J $cm^{-2}$.

Laser induced periodic surface structures emerge as a result of a nonlinear growth process, initiated by the scattering of a fraction of light out of the incident laser beam by randomly distributed irregularities initially present on the irradiated surface. The laser beam itself can also generate these irregularities and therefore we should consider two irradiation regimes. If the laser fluence is only sufficient to locally melt the surface, elevated hillocks will form at first and scattering of light from these features will lead to the formation of periodic stripes. At higher laser fluences, the surface completely melts and the formation of sinusoidal ripples is attributed to various processes such as diffraction, capillary wave formation and feedback mechanisms [17].

Capillary waves have been invoked to explain the formation of solid structures. For a curved liquid-gas interface, a pressure difference is generated. Under the force of surface tension, the created pressure difference supports the deformations in the liquid surface known as capillary waves. Whether these optically pumped capillary waves (particularly in the form of gratings) can be frozen into a solid structure depends on whether the lifetime of the melt is longer than the lifetime of the wave [17].

The formation of ripples is also explainable on the basis of the Kelvin–Helmholtz instability [18]. Microsized ripples are formed, when the laser-induced surface waves are splashed, resolidified, frozen and are permanently imprinted on the ablated surface of the target material [18]. During laser ablation, if the temperature is sufficiently high to melt the surface completely, the molten surface flows in the form of fluid [19]. During the recondensation process the fluid is pulled down due to surface tension. However, the solid–liquid interface still retains the convoluted sinusoidal contour produced by the inhomogeneous deposition of energy at the surface. Thermal conduction causes the underneath cooling of the molten material. The solidification front proceeds upwards which retains the convoluted interface profile [19]. As the resolidification front reaches the target surface, the front becomes restrained, thus effectively breaking the surface into isolated molten pools [20]. The formation of cones is the result of quick solidification of the melted layer. It is attributed to the difference in absorption efficiency of the material in different regions due to voids, inhomogenieties and point defects at the surface relief [21].

The formation of conical structures can be treated as a three step process. First step is the formation of precursor sites, i.e. laser induced nano- and/or microscale structures or the surface defects and roughenesses present before the processing. These sites significantly alter the distribution of irradiated energy on the surface in the second step. The incident laser light scatters off from these sites, resulting in an increased fluence and hence the ablation rate in the valleys between these sites. Finally, these sites evolve into conical structures. The third step is the growth and, possibly, merging of the cones [22]. Thermal ablation on the basis of laser induced heating, thermal desorption, melting and explosive boiling of the target surface is the main reason for extensive material removal as well as formation of pits and cavities [23]. Lu et al. [24] and Yoo et al. [25] reported that for irradiance below some threshold, ablation is governed by normal evaporation while for the irradiances above some threshold, the material is removed by both normal evaporation and explosive boiling. For intensities exceeding $10^9$ W $cm^{-2}$, the sample may be heated above the boiling point and, as a result, a superheated metastable liquid layer can be formed [24, 25]. The liquid at this point is a mixture of vapours and liquid droplets, which results in homogeneous bubble nucleation that facilitate explosive boiling. During multipulse irradiation, a higher pressure is produced due to rapid expansion of microbubbles, which leads to the formation of pits on the Ni surface. The formation of conical pits indicates that the vapour gas remained trapped in the pits [26]. Thermal stresses generated during irradiation are responsible for crack formation [27]. A liquefied material refills cavities, pores and cracks resulting in reduction in their size and number density [28].

SEM images of Fig. 2 demonstrate the morphology of the peripheral ablated area of Ni targets exposed to 1000 laser pulses in vacuum at various fluences. One can see in Fig. 2a the

formation of large-sized irregular shaped grains with distinct grain boundaries. Cracks are also observed along the grain boundaries. Increasing fluence up to 2.5 J $cm^{-2}$ results in a decrease in grain size with more distinct and wider grain boundaries. Pores along grain boundaries are also seen. At a fluence of 2.9 J $cm^{-2}$ (Fig. 2c) the size of the grains decreases and their density increases, the pores disappearing and the grain boundaries becoming more diffusive. At a maximum fluence of 3.4 J $cm^{-2}$ (Fig. 2d), an increase in size of grains is seen along with the appearance of cavities and pores within the grains. The grain boundaries become again more distinct and wider.

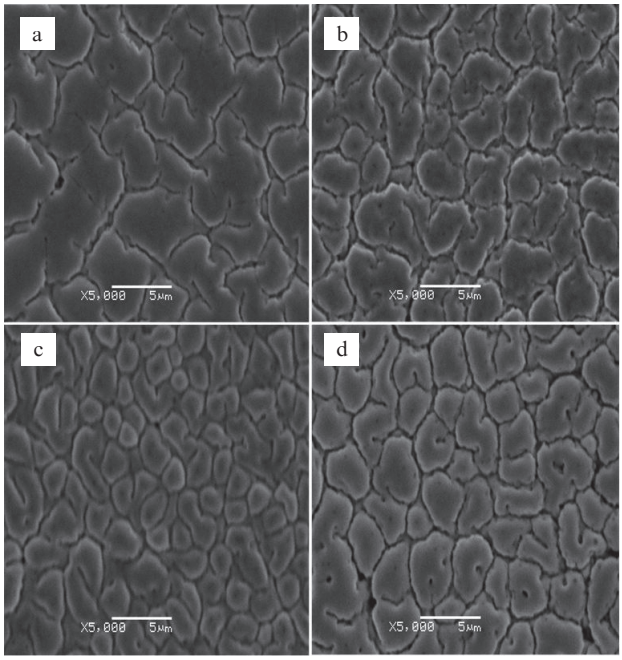


**Figure 2.** SEM images illustrating the formation of laser induced structures at the peripheral ablated area after irradiation of Ni targets in vacuum at laser fluences of (a) 2.1, (b) 2.5, (c) 2.9 and (d) 3.4 J $cm^{-2}$.

Fast melting, cooling and recrystallisation of metal may be a reason for this grain-like surface morphology [29]. Rapid heating and cooling of the target generates thermal and structural residual stresses in the surface layer owing to a large temperature gradient. These thermal and structural stresses are also related to changes in the volume accompanying phase transformations. Therefore, localised heating and cooling lead to predominant crystallisation and grain growth [30]. Melting of the target surface after laser irradiation activates reaction between the molten surface and surrounding media. After laser irradiation recrystallisation takes place and nitrogen disseminates into the surface, which causes more distinct and wider grain boundaries [31].

SEM images of Fig. 3 show the morphology of the central ablated area of Ni targets exposed to 1000 laser pulses in the ambient environment of $N_2$. As compared to vacuum, one observes less distinct diffusive structures. At a fluence of 2.1 J $cm^{-2}$ (Fig. 3a), cones, cavities and less distinct ripples at their base are formed. Increasing fluence up to 2.5 J $cm^{-2}$ (Fig. 3b) leads to an enhanced density of cones and cavities. A further increase in fluence up to 2.9 J $cm^{-2}$ (Fig. 3c) results in the formation of large-sized irregular shaped cavities, whereas

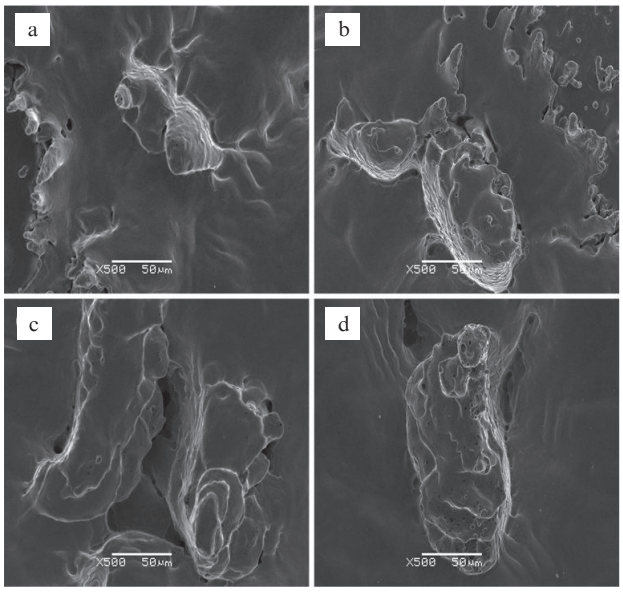


**Figure 3.** SEM images illustrating the formation of laser induced structures at the central ablated area after irradiation of Ni targets in the $N_2$ environment at laser fluences of (a) 2.1, (b) 2.5, (c) 2.9 and (d) 3.4 J $cm^{-2}$.

at a maximum fluence of 3.4 J $cm^{-2}$ (Fig. 3d) highly porous microstructures are formed within ripples.

SEM images of Fig. 4 show the morphology of the peripheral ablated area of Ni targets exposed to 1000 laser pulses in the $N_2$ environment. At a fluence of 2.1 J $cm^{-2}$ (Fig. 4a) there appear a large number of pores, spherical as well irregular shaped pits, wide and large cracks. An increase in fluence up to 2.5 J $cm^{-2}$ (Fig. 4b) results in an increase in the density of cracks along with a decrease in their width and size, whereas the density of pores remains the same. An early stage of formation of grains is also observed. A further increase in fluence up to 2.9 J $cm^{-2}$ (Fig. 4c) causes and increase in the den-

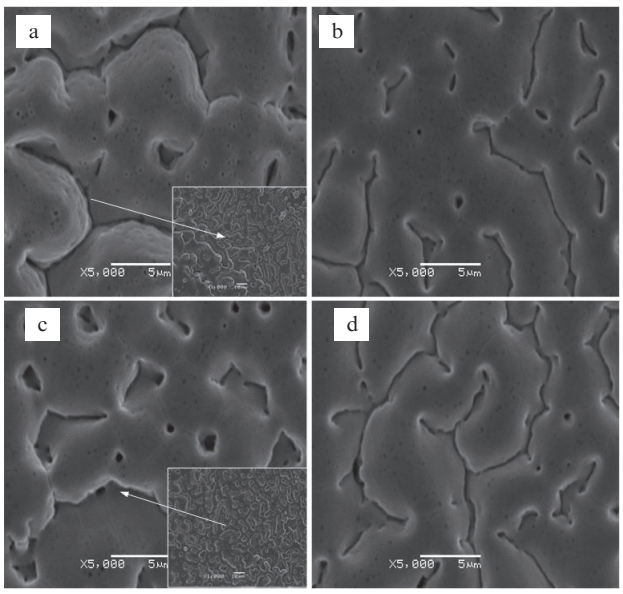


**Figure 4.** SEM images illustrating the formation of laser induced structures at the peripheral ablated area after irradiation of Ni targets in the $N_2$ environment at laser fluences of (a) 2.1, (b) 2.5, (c) 2.9 and (d) 3.4 J $cm^{-2}$.

sity and size of cracks inside the grains. At a maximum fluence of 3.4 J cm$^{-2}$ (Fig. 4d) grain boundaries merge and larger grains with highly porous morphology and enhanced density of distinct and wider cracks are formed.

Thus, the surface morphology of the ablated Ni is significantly different in different environments. During irradiation in vacuum, one observes the formation of protruding conical features with well-defined ripples with an average periodicity of 2 μm and grains with distinct grain boundaries. During irradiation in the $N_2$ environment, grain structures are not well defined and distinct. Grains with pores and conical pits inside the grains cab be seen. Large-sized grains are grown at the peripheral ablated area in the case of $N_2$. Melting of the target surface after laser irradiation activates reaction between the molten surface and surrounding media. After laser irradiation recrystallisation takes place and $N_2$ disseminates into the surface which causes a growth of large grains.

The ambient environment and its pressure play a significant role in the evolution and expansion of laser-induced plasma [32]. It has been observed that shape, size and dynamics of the expanding plume are completely modified by introducing the ambient gas. The physical processes such as confinement effect, shielding effect [33, 34], formation of shock waves [33] and interaction of the plume with an ambient gas depend on the pressure of environment. It has also been reported that the growth of laser induced surface structures is also strongly dependent on the ambient gas nature and pressure [35, 36]. Higher excitation temperatures and densities of generated plasma lead to a greater energy deposition to the lattice of the target and enhance the growth of various micro-/nanostructures on an irradiated surface. Lower pressures (10–50 Torr) of environmental gases offer confinement, which prevents the free expansion of the plume and random movement of an ejected material during laser ablation and stabilises the generation of surface waves, in a well-defined manner [37]. This confinement can induce a higher energy and pressure [38] as compared to vacuum. As the pressure is further increased from 100 to 760 Torr, the confinement effect of the plasma nearer to the target surface becomes more pronounced, which results in a stronger shielding of the target surface [39] and a reduction of the ablated mass from the target [40].

Figure 5 shows Raman spectra of untreated and irradiated Ni samples exposed to 1000 laser pulses in the $N_2$ environment. Raman modes arise on the surface of Ni after irradiation due to the formation of nitrides and oxides on the metal surface. For the irradiated samples two broad peaks are identified at 1323 and 1777 cm$^{-1}$, which correspond to Ni–$NO_2$ and $NO_3^{-1}$ bonds, respectively [41]. The peak at 870 cm$^{-1}$ at a fluence of 2.5 J cm$^{-2}$ corresponds to the N–N bond. With a further increase in fluence up to 2.9 J cm$^{-2}$ this bond dissociates and does not appear in the Raman Spectra. No Raman signal is observed for Ni targets irradiated in vacuum.

We used the XRD data for phase identification and assessment of crystallinity, dislocation densities and residual strains. Phase changes were not observed in vacuum. However, in the $N_2$ environment new phases of nitrides were identified. The variation in spacing $d$, peak intensity and full width at half maximum (FWHM) values were observed for both environments.

The crystallite size $D$ was estimated using Scherer's formula [42]

$$D = 0.9\lambda/(F\cos\theta), \quad (1)$$

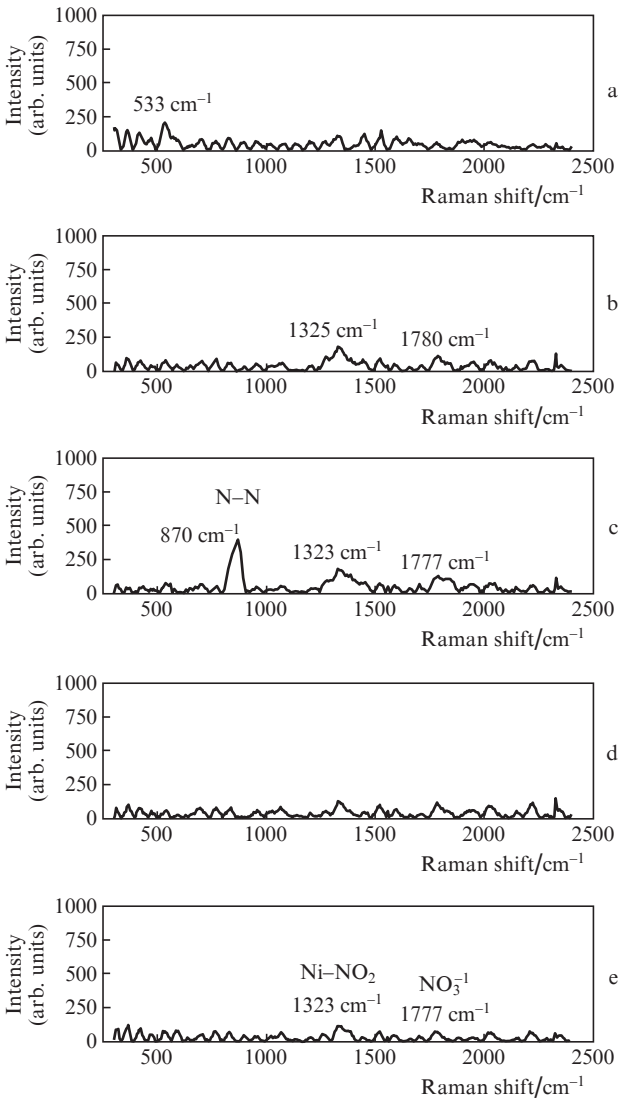


**Figure 5.** Raman spectra for the untreated (a) and irradiated Ni in the $N_2$ environment at laser fluences of (b) 2.1, (c) 2.5, (d) 2.9 and (e) 3.4 J cm$^{-2}$.

where $\lambda = 0.1546$ nm, $F$ and $\theta$ are the X-ray wavelength, diffraction maximum width (FWHM) and Bragg's angle, respectively.

To evaluate the dislocation line density $\delta$ we used the relation [42]

$$\delta = 1/D^2. \quad (2)$$

The residual strain was evaluated by the formula [42]

$$S = 0.9\lambda/(4D). \quad (3)$$

Figure 6 presents the crystallographic data on the untreated and irradiated Ni samples in vacuum. At angles of 44.39° and 51.63° one can observe (Fig. 6a) two diffraction peaks corresponding to (111) and (200) phases. The peak intensity corresponding to the diffraction plane (111) initially decreases with increasing fluence from 2.1 to 2.5 J cm$^{-2}$. The reason for this fact is recrystallisation during resolidification. However, with increasing fluence up to 2.9 J cm$^{-2}$ one can observe an increase in peak intensity, which is attributed to the enhance-

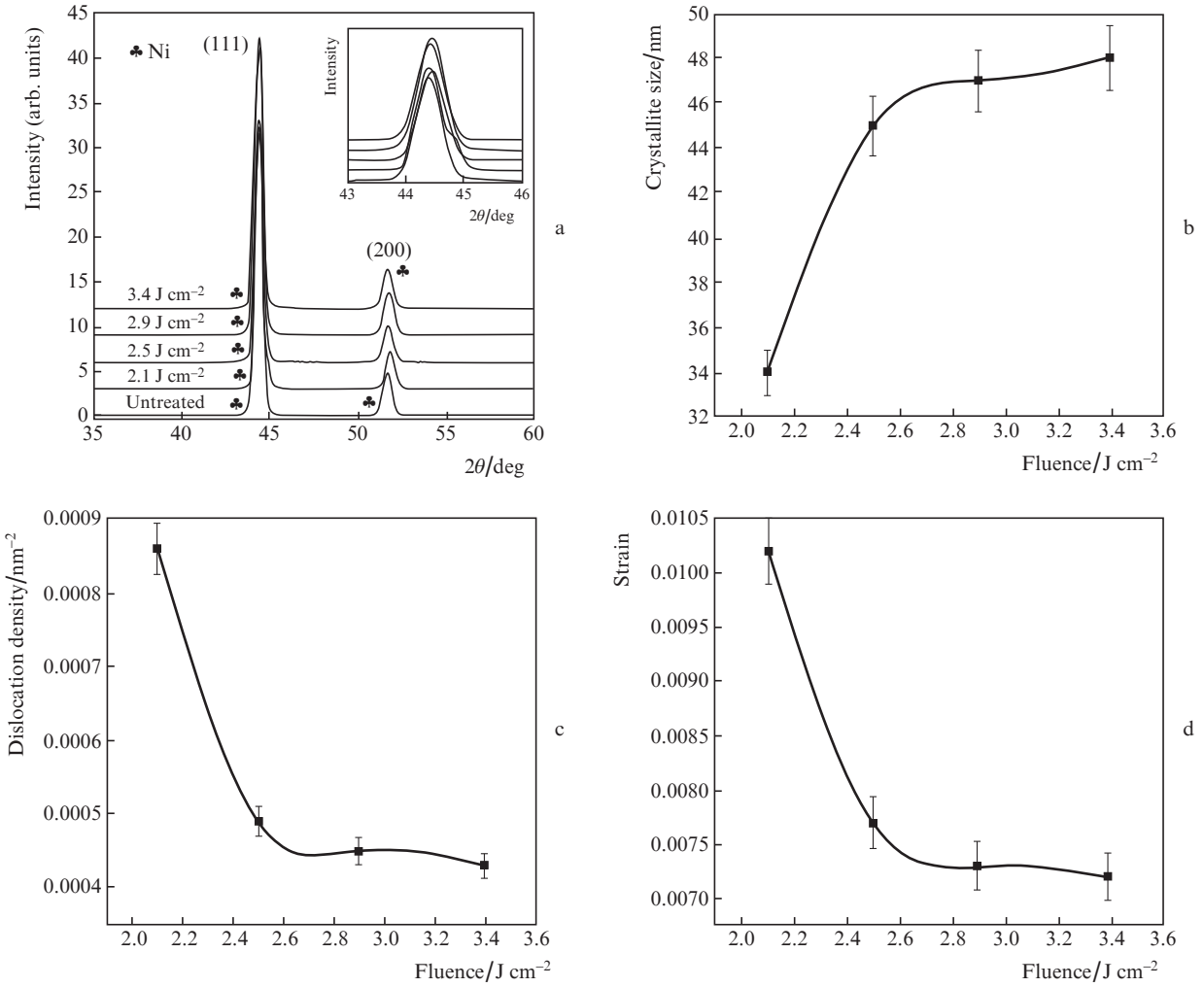


**Figure 6.** XRD data for Ni samples irradiated in vacuum at laser fluences of 2.1, 2.5, 2.9 and 3.4 J cm$^{-2}$: (a) XRD difrractograms, (b) crystallite size, (c) dislocation density and (d) strains.

ment of diffraction of X-rays from target and the crystal growth caused by atomic diffusion across the grain boundaries after laser ablation. At a maximum fluence of 3.4 J cm$^{-2}$, due to fast melting and cooling, the resolidification and recrystallisation processes starts to take place: large-sized grains break up into smaller ones, resulting in a decrease in peak intensity. As the laser beam interacts with the material, the energy deposition initially generates defects, and when energy deposition increases with increasing laser fluence, the defects are annealed. A further increase in laser fluence causes generation of enhanced defects. On the whole, it determines the anomalous behaviour of the diffraction peak intensity.

Figure 6b shows the dependence of the crystallite size on the fluence, estimated by using the data on the diffraction peaks (111) and (200) and formula (1). One can see that the crystallite size increases with increasing laser fluence.

Residual strains and stresses, corresponding to the (111) plane of the Ni crystal, were estimated by formula (3). Changes in dislocation density and stresses after irradiation in vacuum are presented in Figs 6c and 6d. One can see that they decrease with increasing fluence from 2.1 to 3.4 J cm$^{-2}$.

Figure 7 presents the crystallographic data on untreated and irradiated Ni samples in the $N_2$ atmosphere. For the untreated target, two diffraction peaks corresponding to (111) and (200) are observed. For the untreated target the peak identified at an angle of 44.39° corresponds to the phase of crystallised Ni, whereas for irradiated targets this phase is transformed into $Ni_3N$ and new peaks are identified at angles of 44.51°, 44.55° and 44.58° corresponding to the diffraction plane (111) [43].

Compressive and tensile residual stresses are generated on the surface of Ni after laser irradiation, which leads to peak shifting in XRD patterns: the peak shifting towards a higher angular position is an indication of compressive stresses, whereas shifting towards a lower angular position indicates tensile stresses (Fig. 7a). The peak intensity corresponding to the (111) diffraction plane of $Ni_3N$ initially increases with increasing fluence from 2.1 to 2.5 J cm$^{-2}$. However, at a fluence of 2.9 J cm$^{-2}$ a decrease in peak intensity is observed. At a maximum fluence of 3.4 J cm$^{-2}$ the peak intensity decreases. As the laser fluence increases from 2.1 to 2.5 J cm$^{-2}$, solute $N_2$ atoms segregate on the target surface and diffuse across the grain boundaries due to enhanced heat generation and energy deposition. The concentration and diffusion of $N_2$ increase into the material, which is responsible for the increase in intensity of the (111) peak of $Ni_3N$. At a maximum fluence of 3.4 J cm$^{-2}$, due to fast melting and cooling, the resolidification and recrystallisation processes start to take place. The large-sized grains break up into smaller ones, which causes the reduction in peak intensity.

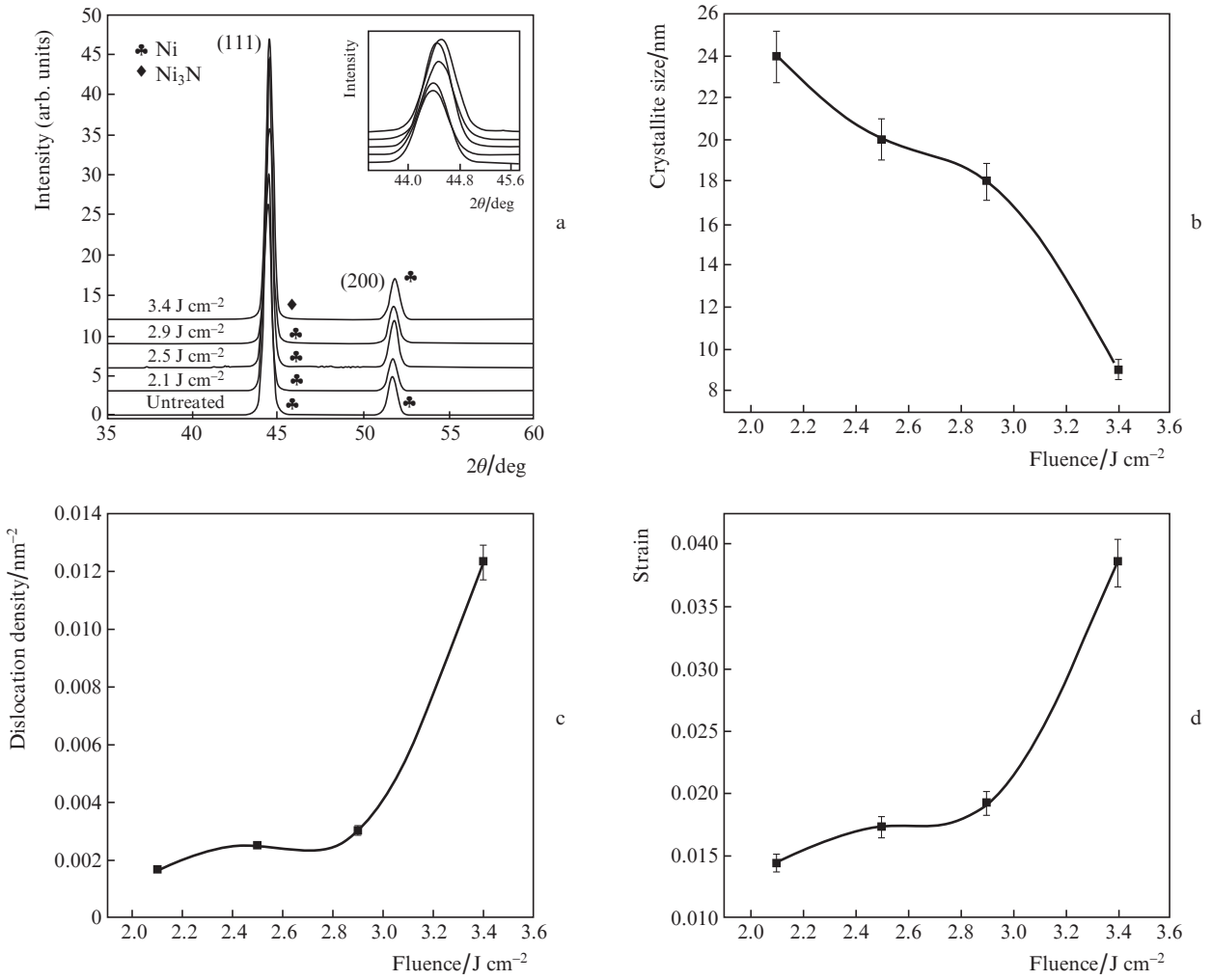


**Figure 7.** XRD data for Ni samples irradiated in the $N_2$ environment at laser fluences of 2.1, 2.5, 2.9 and 3.4 J cm$^{-2}$: (a) XRD difrractograms, (b) crystallite size, (c) dislocation density and (d) strains.

Figure 7b shows the dependence of the crystallite size on fluence. One can see that the crystallite size decreases with increasing laser fluence. Ablated Ni atoms react with gas atoms and redeposit after nitride formation. This process, as that of above-discussed diffusion of nitrogen into nickel, is responsible for the reduction of the crystallite size.

The decrease in crystallite size can be also attributed to the presence of residual stresses and generation of defects. The data shown in Figs 7c and 7d show that the dislocation density and strain increase with increasing fluence.

When the laser beam strikes the material, it causes vaporisation of a thin layer of the material surface. The vaporised species react with the background gas and the rapidly expanding heated gas generates a huge pressure – in the GPa range – on the surface [44]. Recently, Jelani et al. [45] reported generation of this pressure on a zirconium target surface irradiated with a 248-nm, 20-ns KrF excimer laser. This propagating pressure causes the development of high residual compressive stress; however, the enhanced diffusion rate of gas atoms with increasing fluence is the cause for a decrease in residual stresses [46].

An untreated nickel sample shows the hardness of 262 HV. Figure 8 shows the variation in hardness of laser irradiated nickel targets in vacuum as a function of fluence. A continuous

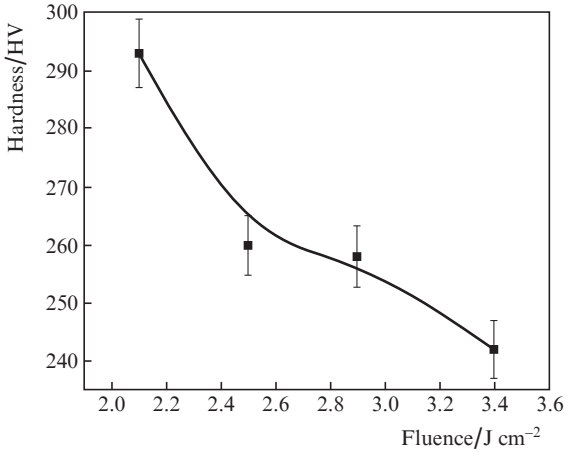


**Figure 8.** Microhardness of Ni samples irradiated in vacuum vs. laser fluence.

decrease in hardness with increasing fluence can be explained by thermal annealing of the surface layer as well as by redeposition and resolidification after melting. In addition, it can be attributed to enhanced tensile residual stresses as well as to

formation of large crystallites. The microstructural defects (see Fig. 1) produced in the targets after irradiation are responsible for the variation in microhardness.

Figure 9 shows the dependence of hardness of Ni after irradiation in the ambient $N_2$ environment on laser fluence. A monotonic increase in hardness of irradiated nickel in this case is attributable to interstitial diffusion of $N_2$ into the lattice, which results in decrease in crystallite size [47]. The smaller crystallite size is efficient in obstructing the dislocation movement and is responsible for a high strength and hardness. Refilling of cracks and cavities (see Figs 2c and 2d), is responsible for an increase in hardness with increasing fluence.

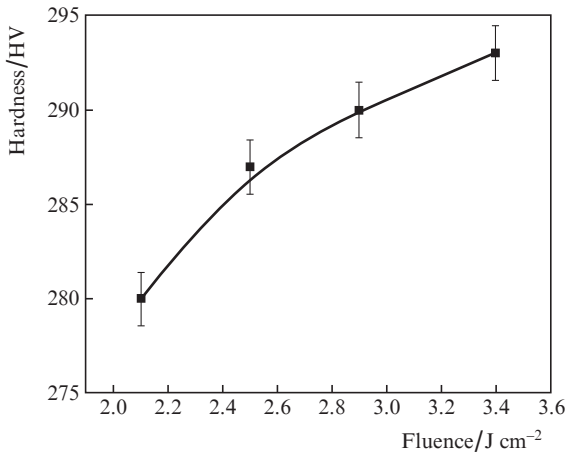


**Figure 9.** Microhardness of Ni samples irradiated in the $N_2$ environment vs. laser fluence.

## 4. Conclusions

The effect of laser fluence on surface, structural and mechanical properties of Ni has been investigated after ablation in the ambient environment of vacuum and $N_2$. Analysis of SEM images shows that laser irradiation in vacuum results in the formation of distinct and well defined features in the form of protruding conical structures, ripples, small sized grains with distinct grain boundaries, irregular shaped cavities and cracks. In the case of irradiation in the $N_2$ environment, less distinct and diffused features in the form of cones, ripples with large-sized grains are formed. Raman spectra of untreated Ni samples and Ni samples irradiated in vacuum and $N_2$ atmosphere show that no Raman bands are identified in the case of vacuum, whereas irradiation in the ambient $N_2$ environment demonstrates that nitrides and nitro-oxides are formed. XRD analysis reveals that no new phases are formed for the Ni ablation in vacuum, while the appearance of $Ni_3N$ is observed in the case of Ni ablation in the $N_2$ atmosphere. The variation in the peak intensity is observed to be anomalous, which is attributed to an increase in crystallite size with increasing fluence for Ni ablated in vacuum. When Ni is ablated in the $N_2$ atmosphere, the crystallite size decreases with increasing fluence. Micro hardness analysis of the targets exposed in vacuum shows a decrease in hardness with increasing fluence. In the case of the $N_2$ environment, a monotonic increase in hardness is observed with increasing fluence. The diffusion of $N_2$ (confirmed by Raman spectroscopy and XRD analysis) across the grain boundaries is considered to be responsible for an increased hardness of the material.

***Acknowledgements.*** The authors thank the Higher Education Commission of Pakistan for providing the funding for the Project 'Up Gradation of Laser facilities at CASP, GCU'. The authors are grateful to the CASP Director, Dr. Riaz Ahmad, for providing the XRD facilities; to Dr. Muhammad Shahid Rafique and Dr. Waheed Anwar from the Department of Physics at the UET Lahore for providing a Raman spectroscope; and to Dr. Tauseef for providing a SEM facility at the CASP.

## References

1. Yong T.K., Tan S.S, Nee C.H., Yap S.S., Kee Y.Y., Sáfrán G., Horváth Z.E., Moscatello J., Yap Y.K., Tou T.Y. *Mater. Lett.*, **66**, 280 (2012).
2. Bashir S., Rafique M.S., Husinsky W. *Nucl. Instrum. Methods B*, **275**, 1 (2012).
3. Kalsoom U., Bashir S., Ali N. *Surf. Coat. Technol.*, **235**, 297 (2013).
4. Dauscher A., Feregotto V., Cordier P., Thorny A. *Appl. Surf. Sci.*, **96-98**, 410 (1996).
5. Karimzadeh R., Anvari J.Z., Mansour N. *Appl. Phys. A*, **94**, 949 (2009).
6. Iyengar V.V., Nayak B.K., Gupta M.C. *Appl. Opt.*, **49**, 5983 (2010).
7. Duley W.W. *UV Lasers Effects and Applications in Materials Science* (New York: Cambridge University Press, 2006).
8. Henley S.J., Poa C.H.P., Adikaari A.A.D.T., Giusca C.E., Carey J.D., Silva S.R.P. *Appl. Phys. Lett.*, **84**, 4035 (2004).
9. Dan L., Ming Z.D. *Chin. Phys. Lett.*, **25**, 1368 (2008).
10. Korolkov V.P., Ionin A. A., Kudryashov S.I., Seleznev L.V., Sinitsyn D.V., Samsonov R.V., Masliy A.I., Medvedev A.Z., Goldenberg B.G. *Kvantovaya Elektron.*, **41**, 387 (2011) [*Quantum Electron.*, **41**, 387 (2011)].
11. Mahmood K., Farid N., Ghauri I.M., Afzal N., Idrees Y., Mubarik F.E. *Phys. Scr.*, **82**, 045606 (2010).
12. Lavisse L., Jouvard J.M., Gallien J.P., Berger P., Grevey D., Naudy P. *Appl. Surf. Sci.*, **254**, 916 (2007).
13. Preuss S., Demchuk A., Stuke M. *Appl. Phys. A*, **61**, 33 (1995).
14. Zuhlke C.A., Anderson T.P., Alexander D.R. *Appl. Surf. Sci.*, **283**, 648 (2013).
15. Liu B., Hu Z., Che Y. *Appl. Phys. Lett.*, **90**, 044103 (2007).
16. Amoruso S., Bruzzese R., Wang X., Nedialkov N.N., Atanasov P.A. *J. Phys. D: Appl. Phys.*, **40**, 331 (2007).
17. Kolasinski K.W. *Curr. Opin. Solid State Mater. Sci.*, **11**, 76 (2007).
18. Lu Y.F., Yu J.J., Choi W.K. *Appl. Phys. Lett.*, **71**, 3439 (1997).
19. Kerr N.C., Omar B.A., Clark S.E., Emmony D.C. *J. Phys. D: Appl. Phys.*, **23**, 884 (1990).
20. Stratakis E., Ranella A., Fotakis C. *Biomicrofluidics*, **5**, 013411 (2011).
21. Mansour N., Jamshidi-Ghaleh K., Ashkenasi D. *J. Laser Micro/Nanoeng.*, **1** (1), 12 (2006).
22. Zuhlke C.A., Anderson T.P., Alexander D.R. *Opt. Express*, **21** (7), 8460 (2013).
23. Oliveira V., Ausset S., Vilar R. *Appl. Surf. Sci.*, **255**, 7556 (2009).
24. Lu Q., Mao S.S., Mao X., Russo R.E. *Appl. Phys. Lett.*, **80**, 3072 (2002).
25. Yoo J.H., Jeong S.H., Greif R., Russo R.E. *J. Appl. Phys.*, **88**, 1638 (2000).
26. Yoo J.H., Jeong S.H., Mao X.L., Greif R., Russo R.E. *Appl. Phys. Lett.*, **76**, 783 (2000).
27. Bashir S., Vaheed H., Mahmood K. *Appl. Phys. A*, **110**, 389 (2013).
28. Ali N., Bashir S., Kalsoom U., Akram M., Mahmood K. *Appl. Surf. Sci.*, **270**, 49 (2013).
29. Hafeez S., Sheikh N.M., Rashid B., Baig M.A. *J. Appl. Phys.*, **103**, 083117 (2008).
30. Farid N., Bashir S., Mahmood K. *Phys. Scr.*, **85**, 01570200 (2012).
31. Mahmood K., Farid N., Ghauri I.M., Afzal N., Idrees Y., Mubarik F.E. *Phys. Scr.*, **82**, 045606 (2010).

32. Khan S., Bashir S., Hayat A., Khaleeq-ur-Rahman M., Faizan-ul-Haq. *Phys. Plasmas*, **20**, 073104 (2013).
33. Giacomo D.A., Dell'Aglio M., Gaudiuso R., Amoruso S., Pascale D.O. *Spectrochim. Acta, Part B*, **78**, 1 (2012).
34. Tognoni E., Palleschi V., Corsi M., Cristoforetti G. *Spectrochim. Acta, Part B*, **57**, 1115 (2002).
35. Farid N., Bashir S., Mahmood K. *Phys. Scr.*, **85**, 015702 (2012).
36. Chen Z., Qiang W., Ming Y., Baiquan T., Jianghong Y., Rupp R.A., Yaan C., Xu J. *Laser Part. Beams*, **13**, 1 (2013).
37. Ganeev R.A., Baba M., Ozaki T., Kuroda H. *J. Opt. Soc. Am. B*, **27**, 1077 (2010).
38. Harilal S.S., Bindhu C.V., Tillack M., Najmabadi F., Gaeris A. *J. Appl. Phys*., **93**, 2380 (2003).
39. Bashir S., Farid N., Mahmood K., Rafique M.S. *Appl. Phys. A*, **107** (1), 203 (2012).
40. Knight K.A., Scherbarth N.L., Cremers D.A., Ferris M.J. *Appl. Spectrosc*., **54**, 331 (2000).
41. Socrates G. *Infrared and Raman Characteristic Group Frequencies* (England: John Wiley & Sons, 2010).
42. Cullity B.D. *Elements of X-ray Diffraction* (London: Addison-Wesley Publishing Company, 1978).
43. Cullity B.D., Stock S.R. *Elements of X-ray Diffraction* (New Jersey: Prentice Hall, 2001).
44. Juodkazis S., Nishimura K., Tanaka S., Misawa H., Gamaly E.G., Luther-Davies B., Hallo L., Nicolai P., Tikhonchuk V.T. *Phys. Rev. Lett*., **96**, 166101 (2006).
45. Jelani M., Bashir S., Khaleeq-ur-Rehman M., Ahmad R., Faizan-ul-Haq, Yousaf D., Akram M., Afzal N., Chaudhry M.U., Mahmood K., Hayat A., Ahmad S. *Eur. Phys. J. D*, **159**, 1 (2013).
46. Corengia P., Ybarra G., Moina C., Cabo A., Broitman E. *Surf. Coat. Technol.*, **200**, 2391 (2005).
47. Yousaf D., Bashir S., Akram M., Kalsoom U., Ali N. *Radiat. Eff. Defects Solids*, **169** (2), 1 (2013).